Open-Phase Fault-Tolerant Pole Transition Control of an Asynchronous Variable-Pole Machine Using Harmonic Plane Decomposition

Yixuan Wu, *Graduate Student Member, IEEE*, Luca Vancini, *Member, IEEE*,
Luca Zarri, *Senior Member, IEEE*, Angelo Tani, and
Luca Peretti, *Senior Member, IEEE*

***Abstract*— Automotive applications are revisiting the use of induction machines (IMs) as magnet-free propulsive solutions due to their intrinsic robustness and reliability. Special multiphase configurations are under investigation to reduce the losses further and fulfill the stringent energy-efficiency and compactness requirements of the automotive industry. One of these configurations is known as variable-pole machines (VPMs), which allows the number of magnetic pole pairs to change on the fly. These machines can stretch the torque-speed operating region, exploit the maximum torque capability, and exhibit competitive efficiency. Although fault tolerance has been widely explored for multiphase machines, the same cannot be said for VPMs, because, until recently, complete models to describe their dynamics under any condition, including magnetic pole changing and fault occurrences, were unavailable. This article presents a post-fault control strategy for VPMs with an open-phase fault (OPF), which can operate during pole changing and address the issue of fault-tolerant operation. The effectiveness of the control system is verified by experimental tests carried out with an 18-phase variable-pole IM prototype.**

***Index Terms*— Fault tolerance, multiphase electric machines, post-fault operation, variable phase-pole machine.**

NOMENCLATURE

Subscripts and Superscripts

x^{T}	Matrix transformation.
x^{ref}	Reference value.
x_R	Rotor variables in the inverse-Γ model.
x_r	Rotor variables.
x_s	Stator variables.
x_{123}	Variables in the fundamental reference frame.
$x_{\alpha\beta 0}$	Variables in the stationary $\alpha\beta 0$ reference frame.
x_σ	Leakage quantity in the inverse-Γ model.
x_{dq0}	Variables in the rotating $dq0$ reference frame.
x_h	Harmonic plane.
x_M	Magnetizing quantities in the inverse-Γ model.

Variables

$\bar{\alpha}$	Complex number representing pitch angle between two neighboring minimum windings.
δ	Pitch angle of the minimum winding.
$\mathbf{C}_{[.]}$	Core Clarke transformation matrix.
$\mathbf{T}_{a\rightarrow b}$	Transformation matrix from a to b.
$\mathbf{x}_{[.]}$	Space vector quantity in [.] reference frame.
ω_0	Resonant angular frequency of a PIR controller.
ω_c	Cutoff angular frequency of a PIR controller.
ω_m	Rotor mechanical angular speed.
ω_s	Stator electric angular frequency.
ψ	Flux linkage.
τ_{shaft}	Shaft torque.
τ_e	Machine torque.
θ_h	Park transformation angle in harmonic plane h.
$\theta_{s/r}$	Stator or rotor angle.
ϑ	Angle for rotor Clarke transformation matrix.
ϑ_{h,k_f}	Phase angle of the magnetic axis of the faulty phase k_f in harmonic plane h.
ξ	Largest odd number smaller or equal to m.
G_{PIR}	Transfer function of the PIR controller.
h	Harmonic plane order.
i	Current.
k_f	Faulty winding.
K_p, K_i, and K_r	Controller gains of the PIR controller.
L and R	Inductance and resistance.
m	Number of phases.
n_{mw}	Number of minimum windings.

Manuscript received 23 January 2024; revised 5 April 2024; accepted 27 April 2024. Date of publication 3 May 2024; date of current version 2 August 2024. This work was supported in part by the "STandUP for Energy" at KTH Royal Institute of Technology; and in part by the National Recovery and Resilience Plan (NRRP), Mission 4 Component 2 Investment 1.3—Call for tender No. 1561 of 11.10.2022 of Ministero dell'Università e della Ricerca (MUR), through European Union—NextGenerationEU under Award PE0000021, and through Concession Decree No. 1561 of 11.10.2022 adopted by Ministero dell'Università e della Ricerca (MUR), CUP, project title "Network 4 Energy Sustainable Transition—NEST" under Grant J33C22002890007. Recommended for publication by Associate Editor Dian Guo Xu. *(Corresponding author: Luca Zarri.)*

Yixuan Wu and Luca Peretti are with the Division of Electric Power and Energy Systems, KTH Royal Institute of Technology, 100 44 Stockholm, Sweden (e-mail: yixuanw@kth.se; lucap@kth.se).

Luca Vancini, Luca Zarri, and Angelo Tani are with the Department of Electrical, Electronic and Information Engineering "Guglielmo Marconi," University of Bologna, 40136 Bologna, Italy (e-mail: luca.vancini4@unibo.it; luca.zarri2@unibo.it; angelo.tani@unibo.it).

Color versions of one or more figures in this article are available at https://doi.org/10.1109/JESTPE.2024.3396722.

Digital Object Identifier 10.1109/JESTPE.2024.3396722

p	Number of pole pairs.
$P_{\mathrm{cu},s}$	Stator copper losses.
p_{mw}	Number of pole pairs for the minimum winding configuration.
Q_s and Q_r	Number of stator and rotor slots.
s	Laplace variable.
v	Voltage.
v_{dc}	DC-link voltage.

I. INTRODUCTION

VARIABLE-POLE machines (VPMs), as a subcategory of multiphase electrical machines (MPEMs) [1], [2], [3], [4], are gaining popularity in applications where the torque-speed demand is very wide, such as traction applications [1], [2], [3], [4]. VPMs are induction machine (IM)-based systems that can electronically change the number of pole pairs on the fly without hardware reconfiguration, such as an electric gearbox. The different phase-pole configurations (PPCs) allow the fulfillment of the drive cycle demands with the potential to be equally or more efficient than synchronous machine counterparts [5]. Fig. 1 qualitatively summarizes the enlarged operation area of VPMs. Their characteristics fit well with two main demands of typical traction applications [5], [6].

1) High torque at low speeds can be provided by configurations with a high number of pole pairs.
2) High efficiency at high speeds and low torque can be provided by configurations with a low number of pole pairs.

A study using finite-element (FE) simulations shows that a VPM is smaller than a fixed-pole IM, for the same driving cycle demand of a long-haul truck [7]. Other FE simulations show that VPMs can achieve high efficiency, especially in cruising operations [8], [9].

There are different VPM designs in the literature, e.g., starter generators that use six-phase IMs to provide high-torque capability for short periods at low speed for cranking [10], [11] or propulsion motors with toroidal single-slot stator windings [12], [13], [14]. Regardless of the design, the absence of a modeling approach that could describe the behavior of VPMs during a pole-phase reconfiguration was a major drawback. This issue was addressed in [15] and [16], where a unified model independent of the PPC was presented as a solution for modeling and controlling the VPMs. In this approach, called harmonic plane decomposition (HPD), individual spatial harmonics are modeled and controlled, thus shaping the magneto-motive force (MMF) distribution of different PPCs with a control structure independent of the PPC.

The next step in VPM drive development is to include fault-tolerant features. Heavy-duty electric vehicles require a higher level of reliability as unscheduled downtime and cost of ownership are major concerns. In the event of a fault, it is important to have a "limp-home" operation until proper maintenance can be carried out, which can significantly reduce costs compared with an immediate shutdown. In simpler terms, the vehicle should be able to travel to the nearest workshop instead of stopping immediately.

The inherent multiphase configuration of VPMs offers additional degrees of freedom, which can be exploited to increase the torque density and the energy efficiency of the entire drive [17], [18], [19]. These additional degrees of freedom potentially enable true fault tolerance (TFL), which for VPMs means the following.

1) Constant torque must be exerted even in the event of a fault.
2) The drive can retain the pole-changing capability to achieve the enlarged mechanical operation area.

This article analyzes the issue of open-phase faults (OPFs), which are more likely to occur in a VPM due to the increased number of individual phases. With more terminals and inverter legs exposed to mechanical failures, internal winding ruptures, welding problems, or converter electrical faults, OPFs are a major concern in power systems [20].

The literature shows different approaches to post-fault controllers (PFCs) in IM-based MPEMs [4]. Either a model of the healthy machine or a reduced-order model of the faulty machine may be used. The reduced-order model may require adapting the transformation matrix and the modulation strategy [21]. Also, switching from the healthy model to the faulty model creates a discontinuity.

Following the idea of model continuity, the healthy model is more advisable for VPMs [15], [16], but the faulty operation requires injecting a compensating current into the non-excited harmonic planes. However, the assumption of perfect sinusoidal windings does not hold for VPMs. A deeper analysis of the post-fault current references shows three different optimal strategies, i.e., minimum copper loss, minimum peak current, and minimum torque ripple [22], [23].

Many implementations are possible for the controllers regulating the post-fault currents [4]: hysteresis control, fuzzy logic or sliding mode control, model predictive control (MPC), and dual PI or PR control. The last two are most suitable for a PFC with a healthy model, especially due to their simple implementation. The idea of combining them into a proportional-integral-resonant (PIR) controller seems natural, so this solution has already been used for a PFC with minimum torque ripple [23]. For completeness, it is worth noting that direct torque control (DTC) may also be applied for a PFC with a two-level [24] or three-level inverter [24].

The focus of this article lies on the pole-changing capability under faulty conditions. To the best of authors' knowledge, no literature investigates this aspect.

If pole changing was not possible during fault conditions, the drive would lose a significant part of the operating range illustrated in Fig. 1. Therefore, this article illustrates the structure of a PFC with current injection for a VPM. Furthermore, the current reference for pole transition ensures the fault-tolerant operation with minimum copper losses. The analysis is based on the HPD, which is briefly described in Section II. Section III describes the fault-tolerant strategy for an OPF. Section IV illustrates its implementation using PIR controllers. Section V presents the experimental validation performed on an 18-phase VPM. Both steady-state performance and dynamic performance are shown for pole reconfiguration to demonstrate the validity of the developed approach.

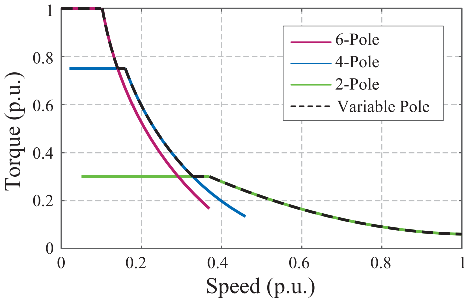

Fig. 1. Torque-speed characteristics for two-, four-, and six-pole configurations of a given VPM.

II. Harmonic Plane Decomposition Model

The HPD theory provides the foundation for modeling a VPM [15], [16]. In contrast to the state-of-the-art vector-space decomposition (VSD), where the rank of the model is dependent on the number of phases, the HPD creates a unified model for all possible PPCs of a VPM, thus facilitating the pole transitioning control.

A. Transformation Matrices

Utilizing the 123 fundamental reference frame is advantageous for MPEMs with multiple PPCs, such as VPMs, because it is not influenced by the hardware connections or the PPC [25]. The magnetic axes of the practical *abc* reference frame are mapped into axes with phase angles in the range $[0, \pi)$ for the 123 fundamental reference frame.

The model dimension depends on the number n_{mw} of minimum (or elementary) windings, which can be regarded as building blocks. For example, Fig. 2 shows the distribution of the magnetic axes in the 123 fundamental reference frame for an IM with $n_{\mathrm{mw}} = 18$. From now on, n_{mw} is assumed even.

The Clarke transformation matrix for the VPM from the 123 fundamental reference frame to the $\alpha\beta0$ stationary reference frame is shown in (1), as shown at the bottom of the page, [15], [16].

The generalization of the Park transformation, which transforms a space vector $\mathbf{x}_{\alpha\beta0}$ from the stationary $\alpha\beta0$ reference frame to the synchronous $dq0$ reference frame, is represented by the block diagonal matrix (2), such that the main-diagonal blocks are 2×2 square matrices and all off-diagonal blocks are zero matrices

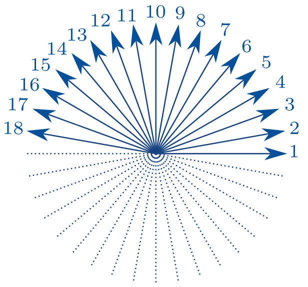

Fig. 2. Distribution of the winding magnetic axes in the fundamental 123 reference frame.

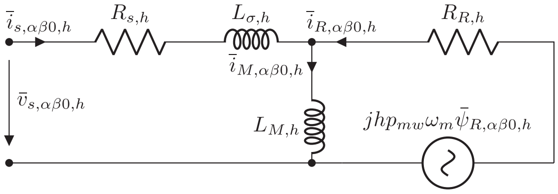

Fig. 3. Inverse-Γ circuit in harmonic plane h in the stationary $\alpha\beta0$ reference frame.

$$\mathbf{T}_{\alpha\beta0\rightarrow dq0} = \begin{bmatrix} a_{1,1} & \dots & a_{1,n_{\mathrm{mw}}} \\ \vdots & \ddots & \vdots \\ a_{n_{mq},1} & \dots & a_{n_{\mathrm{mw}},n_{\mathrm{mw}}} \end{bmatrix}$$

$$\left.\begin{aligned} a_{h,h} &= a_{h+1,h+1} = \cos(\theta_h) \\ a_{h,h+1} &= -a_{h+1,h} = \sin(\theta_h) \end{aligned}\right\} \quad \forall\, h = 1, \dots, n_{\mathrm{mw}}. \tag{2}$$

Since the harmonic planes are independent, the angle θ_h of rotation in each harmonic plane depends on the field-oriented control strategy.

B. Model Equations

The equivalent circuits of each harmonic plane, shown in Fig. 3, can be defined by using the Clarke transformation in the HPD theory

$$\begin{aligned} \frac{\mathrm{d}\bar{\psi}_{s,\alpha\beta0,h}}{\mathrm{d}t} &= \bar{v}_{s,\alpha\beta0,h} - R_{s,h}\bar{i}_{s,\alpha\beta0,h} \\ \frac{\mathrm{d}\bar{\psi}_{R,\alpha\beta0,h}}{\mathrm{d}t} &= jhp_{\mathrm{mw}}\omega_m\bar{\psi}_{R,\alpha\beta0,h} - R_{R,h}\bar{i}_{R,\alpha\beta0,h} \\ \bar{\psi}_{s,\alpha\beta0,h} &= L_{M,h}\bar{i}_{M,\alpha\beta0,h} + L_{\sigma,h}\bar{i}_{s,\alpha\beta0,h} \\ \bar{\psi}_{R,\alpha\beta0,h} &= L_{M,h}\bar{i}_{M,\alpha\beta0,h} \\ \bar{i}_{M,\alpha\beta0,h} &= \bar{i}_{s,\alpha\beta0,h} + \bar{i}_{R,\alpha\beta0,h}. \end{aligned} \tag{3}$$

$$\mathbf{x}_{\alpha\beta0} = \underbrace{\left(\frac{2}{n_{\mathrm{mw}}}\right)\mathbf{C}_s}_{\mathbf{T}_{123\rightarrow\alpha\beta0}} \cdot \mathbf{x}_{123} \qquad \mathbf{x}_{123} = \underbrace{\mathbf{C}_s^{\mathrm{T}}}_{\mathbf{T}_{\alpha\beta0\rightarrow123}} \cdot \mathbf{x}_{\alpha\beta0} \quad \Bigg| \quad \mathbf{C}_s = \begin{bmatrix} 1 & \cos(1\delta) & \cos(2\delta) & \dots & \cos((n_{\mathrm{mw}}-1)\delta) \\ 0 & \sin(1\delta) & \sin(2\delta) & \dots & \sin((n_{\mathrm{mw}}-1)\delta) \\ 1 & \cos(3\delta) & \cos(6\delta) & \dots & \cos((n_{\mathrm{mw}}-1)3\delta) \\ 0 & \sin(3\delta) & \sin(6\delta) & \dots & \sin((n_{\mathrm{mw}}-1)3\delta) \\ \vdots & \vdots & \vdots & \ddots & \vdots \\ 1 & \cos(n_{\mathrm{mw}}\delta) & \cos(2n_{\mathrm{mw}}\delta) & \dots & \cos((n_{\mathrm{mw}}-1)n_{\mathrm{mw}}\delta) \\ 0 & \sin(n_{\mathrm{mw}}\delta) & \sin(2n_{\mathrm{mw}}\delta) & \dots & \sin((n_{\mathrm{mw}}-1)n_{\mathrm{mw}}\delta) \end{bmatrix} \quad \Bigg| \quad \delta = \frac{\pi}{n_{\mathrm{mw}}} \tag{1}$$

The torque equation of VPMs in HPD is as follows:

$$\tau_e = \frac{n_{\text{mw}}}{2p_{\text{mw}}} \sum_h h\bar{\psi}_{R,\alpha\beta0,h} \cdot \bar{i}_{s,\alpha\beta0,h} \tag{4}$$

where the dot product operator "·" of two vectors is defined as the real part of the product between the former vector and the complex conjugate of the latter.

Since the HPD shares the same mathematical roots as the VSD, similar assumptions can be applied. These include magnetic linearity and negligible interplane cross coupling. Therefore, the harmonic planes can be considered independent [26]. As the remaining part of this article focuses only on the stator quantities, the subscript "s" will be omitted in all stator currents and voltages for simplicity.

III. OPEN-PHASE FAULT

When an OPF occurs in the k_fth winding ($k_f \in \{1, 2, \ldots, n_{\text{mw}}\}$), the corresponding current becomes zero, and the following constraint must be satisfied:

$$i_{k_f} = \sum_{h=1,3,\ldots}^{n_{\text{mw}}-1} \bar{i}_{\alpha\beta0,h} \cdot \bar{\alpha}^{h(k_f-1)} = 0, \quad \bar{\alpha} = e^{j\frac{\pi}{n_{\text{mw}}}}. \tag{5}$$

The consequence is that the space vectors of the stator currents $\bar{i}_{\alpha\beta0,h}$ ($h = 1, 3, \ldots, n_{\text{mw}} - 1$) are not independent anymore. However, to preserve the motor operation during the OPF, it is necessary to maintain the same MMF distribution in healthy and faulty conditions. Since this depends on the torque-producing harmonic plane p that is currently excited, the current reference, $\bar{i}^{\text{ref}}_{\alpha\beta0,p}$, must not be altered. During the fault, (5) cannot be fulfilled if the current references in all other non-excited harmonic planes are zero. In other words, to satisfy (5) and maintain the same operating conditions, at least one current space vector $\bar{i}_{\alpha\beta0,h}$ in a harmonic plane other than plane p must not be zero. Many solutions to (5) that keep the MMF and, thus, $\bar{i}^{\text{ref}}_{\alpha\beta0,p}$ unaltered are possible. This article considers the common solution that minimizes the stator copper losses in the post-fault operation [22]. From (5), it is possible to express the current space vectors of the non-excited harmonic planes ($h \neq p$) in terms of the excited harmonic plane ($h = p$) as follows:

$$\sum_{\substack{h=1,3,\ldots\\h\neq p}}^{n_{\text{mw}}-1} \bar{i}_{\alpha\beta0,h} \cdot \bar{\alpha}^{h(k_f-1)} = -\bar{i}^{\text{ref}}_{\alpha\beta0,p} \cdot \bar{\alpha}^{p(k_f-1)}. \tag{6}$$

The instantaneous stator copper losses, expressed in terms of space vectors, can be calculated as follows:

$$P_{\text{cu},s} = \frac{n_{\text{mw}}}{2} R_s \sum_{h=1,3,\ldots}^{n_{\text{mw}}-1} |\bar{i}_{\alpha\beta0,h}|^2. \tag{7}$$

Therefore, to minimize the stator copper losses, it is necessary to minimize the sum of the squared modules of each stator current space vector. To calculate the minimum value, it is convenient to decompose each reference current space vector $\bar{i}_{\alpha\beta0,h}$ into two components (X and Y)

$$\bar{i}_{\alpha\beta0,h} = i_{h,X}\bar{\alpha}^{h(k_f-1)} + j i_{h,Y}\bar{\alpha}^{h(k_f-1)}. \tag{8}$$

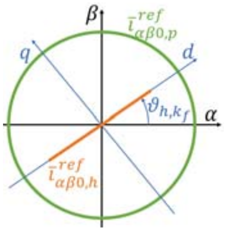

Fig. 4. Trajectories of the stator current space vectors during the fault in steady-state conditions.

Substituting (8) into (6) leads to the following equation:

$$\sum_{\substack{h=1,3,\ldots\\h\neq p}}^{n_{\text{mw}}-1} i_{h,X} = -\bar{i}^{\text{ref}}_{\alpha\beta0,p} \cdot \bar{\alpha}^{p(k_f-1)}. \tag{9}$$

As can be seen, the Y components disappear in (9), so they are set to zero to minimize (7), and it is only necessary to determine the X component of $\bar{i}_{\alpha\beta0,h}$ with $h \in \{1, 3, \ldots, n_{\text{mw}} - 1\}$. It can be verified that the optimal solution is when all the components are equal. Thus, the resulting space vectors of the reference currents in the $\alpha\beta0$ stationary reference frame for the non-excited harmonic planes are as follows:

$$\bar{i}^{\text{ref}}_{\alpha\beta0,h} = -\frac{2}{n_{\text{mw}} - 2}\left(\bar{i}^{\text{ref}}_{\alpha\beta0,p} \cdot \bar{\alpha}^{p(k_f-1)}\right)\bar{\alpha}^{h(k_f-1)}$$
$$\forall h \in \{1, 3, \ldots, n_{\text{mw}} - 1\} \text{ and } h \neq p. \tag{10}$$

In steady-state conditions, the current space vector $\bar{i}_{\alpha\beta0,p}$ must rotate on a circular trajectory with a constant angular frequency $\omega_{s,p}$ even during a fault. As shown in Fig. 4, the current space vectors $\bar{i}_{\alpha\beta0,h}$ ($h \neq p$) move along segments with directions ϑ_{h,k_f} equal to

$$\vartheta_{h,k_f} = h\frac{\pi}{n_{\text{mw}}}(k_f - 1) \tag{11}$$

where ϑ_{h,k_f} is a function of the harmonic plane order h and the index k_f of the faulty winding.

Finally, it is noted that the same strategy for open-fault detection applies to OPFs and open-switch faults (OSFs) [27]. Similarly, the presented fault-tolerant pole-transition strategy can be applied to OSFs.

IV. CONTROL SCHEME

Fig. 5 depicts the structure of the proposed post-fault control system in all harmonic planes. Area (a) refers to the torque-producing harmonic plane p, and area (b) refers to the generic non-torque-producing harmonic plane h ($h \neq p$) in post-fault operation. In the torque-producing plane p, the motor speed is adjusted by a PI controller, which generates a torque request. Depending on the rotor flux level and the desired torque, the control system calculates the reference current vector $\bar{i}^{\text{ref}}_{dq0,p}$, which is tracked by PI controllers in the $dq0$ reference frame synchronous with the rotor flux. The angular frequency $\omega_{s,p}$ is calculated by an observer, i.e., the so-called modified current-voltage model (MCVM) [28].

The space vectors of the reference currents $\bar{i}^{\text{ref}}_{\alpha\beta0,h}$ ($h \neq p$) in the non-excited harmonic planes, which do not contribute to the electromagnetic torque (non-torque-producing planes),

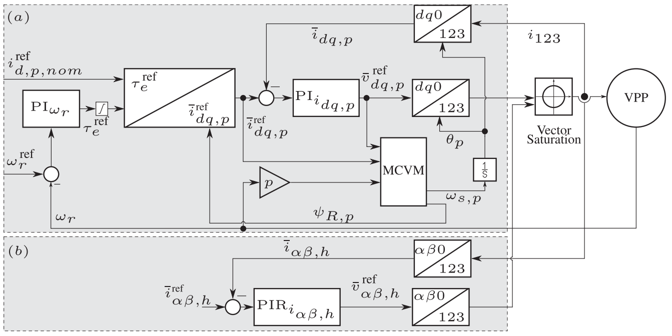

Fig. 5. Full speed and current control structure in post-fault operation for (a) torque-producing harmonic plane p and (b) non-torque-producing harmonic plane $h \neq p$.

are calculated, as explained in Section III. As the references $\bar{i}^{\text{ref}}_{\alpha\beta 0,h}$ are pulsating on straight lines, removing the Park transformation and using a PIR controller simplify the implementation compared with the dual PI controllers.

Since the analysis of the fault angles in (11) is independent of the excited harmonic plane p, the post-fault analysis holds even during a pole transition [15]. During a transition from p_1 to p_2 pole pairs, both harmonic planes p_1 and p_2 are excited simultaneously. Hence, the current references for the non-excited harmonic planes must contain the pulsating currents for both numbers of pole pairs p_1 and p_2. Moreover, if the number of non-excited harmonic planes decreases, the fault current must be distributed among fewer planes. As a result, the current references in the non-excited harmonic planes become

$$\bar{i}^{\text{ref}}_{\alpha\beta 0,h} = \frac{-2}{n_{\text{mw}} - 4}\Big(\bar{i}^{\text{ref}}_{\alpha\beta 0,p_1} \cdot \bar{\alpha}^{p_1(k_f-1)} + \bar{i}^{\text{ref}}_{\alpha\beta 0,p_2} \cdot \bar{\alpha}^{p_2(k_f-1)}\Big)\bar{\alpha}^{h(k_f-1)} \quad \text{if } h \neq p_1 \text{ and } h \neq p_2. \tag{12}$$

It is noted that the proposed PFC only affects the non-excited harmonic planes and does not interfere with the pole-changing strategy. This method keeps the computational burden limited as the online calculation of the transformation angles is unnecessary for all non-excited harmonic planes, especially if compared to the control system with two PI controllers and two Park transformations for the positive and negative sequences per harmonic plane [4], [22], [23]. Since $\bar{i}^{\text{ref}}_{\alpha\beta 0,h}$ is a combination of sinusoidal signals, a PIR controller with two resonant frequencies must be used to achieve zero error at steady state. Its transfer function is as follows:

$$G_{\text{PIR}} = K_p + \frac{K_i}{s} + \frac{2K_r\omega_{c,1}}{s^2 + 2\omega_{c,1}s + \omega_{0,1}^2} + \frac{2K_r\omega_{c,2}}{s^2 + 2\omega_{c,2}s + \omega_{0,2}^2}. \tag{13}$$

The resonant frequencies of the PIR controller are dynamically tuned depending on the stator angular frequency, so that $\omega_{0,1} = \omega_{s,p_1}$ and $\omega_{0,2} = \omega_{s,p_2}$. The forward open-loop transfer function can be used to prove the stability of these controllers [29]. Furthermore, PIR controllers have shown their suitability for PFC in the case without pole transition [23].

However, the omission of the Park transformation has the limitation that multiple OPFs or other fault-tolerant strategies lead to reference current space vectors that do not pulsate and, thus, require a different implementation of the control system [22], [23].

TABLE I

INVERSE-Γ MODEL ELECTRICAL PARAMETERS OF THE VPM[1]

h	1	3	5	7	9	11	13	15	17
R_s	636	636	636	636	636	636	636	636	636
L_σ	11.2	8.4	7.6	7	7	7	7	13.4	12
L_M	310	33	10.8	6.4	6.4	6.4	6.4	-	-
R_R	406	202	136	106	106	106	106	-	-

[1] Resistances in $\text{m}\Omega$. Inductances in mH.

TABLE II

ORIGINAL MACHINE *3GAA161420-BDG* [31] NAME PLATE DATA

P_n [kW]	ω_n [rpm]	I_n [A]	V_n [V]	$\cos\phi$	τ_n [Nm]	f [Hz]
15	2934	15.1	690	0.9	48.8	50

V. EXPERIMENTAL RESULTS

In this section, experimental tests are carried out on a prototype VPM in steady-state operation and during a pole transition under an OPF in the second winding ($k_f = 2$). Table I lists the electrical parameters of the VPM obtained with an offline parameter estimation method designed explicitly for MPEMs [30]. The prototype of the VPM is a modified three-phase two-pole IM, with its original parameters listed in Table II. It is noted that, the machine is a reconfigured three-phase IM, so it is not optimized to operate as a VPM. Nevertheless, although maximum power and efficiency are affected, the prototype can be considered a proof of concept.

A. Experimental Setup

The prototype has 36 independent toroidal slot windings ($Q_s = 36$) and 28 rotor bars ($Q_r = 28$). Each phase of the machine, composed of two opposing toroidal slot windings in series, is fed by a full-bridge converter. The entire inverter consists of 36 two-level legs fed from a common dc voltage. Each leg includes a current measurement as feedback through an *AD9249* ADC [32]. A *Zynq ZC706 Evaluation Kit* [33] performs the centralized control at $f_{\text{PWM}} = 8.00$ kHz. Clocking, ADC deserialization, carrier-based PWM, and low-level communication are implemented in the FPGA. *Core0* implements the control system, while *Core1* runs an Ethernet server for data logging and communication.

The VPM is a two-pole 18-phase IM in the base configuration ($n_{\text{mw}} = 18$) supplied by 18 full bridges. Fig. 6 shows a schematic of the hardware configuration. The OPF is obtained in the faulty winding by opening a breaker in series with it.

Fig. 7 shows the test bench with the VPM, its encoder, and the torque transducer (*Magtrol TM312* [34] and *Magtrol 3411 Torque Display* [35]). The data from the torque transducer are recorded using a *Tektronix 3 Series MDO* [36].

1) Steady-State Operation: The machine is operated in two PPCs, [$m = 18$, $p = 1$] and [$m = 6$, $p = 3$], as summarized in Table III. Table IV lists the tuning gains of the PIR controllers.

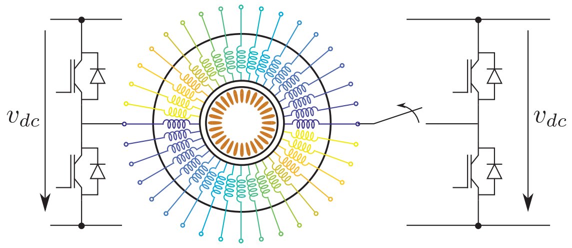

Fig. 6. Schematic of the VPM with 36 toroidal stator windings connected to form 18 phases and 28 rotor bars. Only one inverter leg is shown for clarity. The OPF is induced by a breaker in the faulty winding.

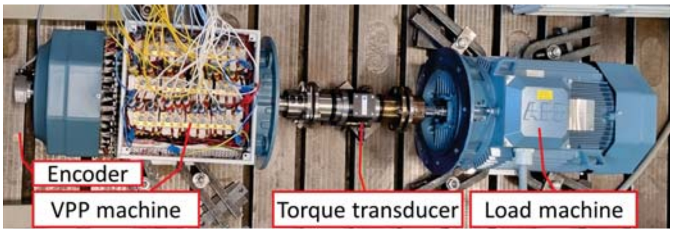

Fig. 7. VPP with load machine.

TABLE III
OPERATIONAL POINTS FOR THE TWO PRESENTED PPCS

Configuration	$i^{\text{ref}}_{d,h=1}$	$i^{\text{ref}}_{d,h=3}$	v_{dc}	ω_m	τ_{shaft}
$[m = 18, p = 1]$	1.8 A	0 A	110 V	1000 rpm	10 Nm
$[m = 6, p = 3]$	0 A	5.4 A	110 V	1000 rpm	10 Nm

TABLE IV
CONTROLLER GAINS OF THE PIR-PFC

h	1	3	5	7	9	11	13	15	17
K_p	35	32	30	14	13	12	11	5	5
K_i	2000	1836	1720	40	40	40	40	120	120
K_r	36	32	28	24	20	16	12	8	4

Gains K_p and K_i are chosen to achieve the desired rise time, and K_r is determined empirically. The cutoff frequency is set to $\omega_c = 0.2\pi$ rad/s, while the resonant frequency $\omega_{0,h}$ $(h \neq p)$ is $\omega_{s,p}$.

2) Pole Transition: The performance of the drive is analyzed during a pole transition from configuration $[m = 18, p = 1]$ to configuration $[m = 6, p = 3]$. The pole transition strategy is the premagnetization method with an instantaneous q-current switch, as described in [15]. The controllers of the VPM drive use the same gains as in the steady-state tests.

B. Analysis of the Experimental Results

1) Steady-State Operation: The time-domain currents i_{123} of windings $[1, 2, 9]$, τ_{shaft}, and ω_r are shown in Fig. 8 for the PPCs with $p = 1$ and $p = 3$. The VPM operates in speed control with $\omega_r^{\text{ref}} = 1000$ r/min, and the load drive applies a torque of $\tau_{\text{shaft}} = 10.0$ Nm. First, the VPM is in healthy mode. Then, an OPF in the second winding $(k_f = 2)$ occurs, and the drive continues with the control strategy for the healthy mode. Finally, the drive switches to the proposed post-fault control strategy. The time instant in which the OPF occurs and the beginning of the proposed fault-tolerant operation are marked. After the OPF happens, the currents become significantly imbalanced. This behavior is visible in the waveform of i_1 shown in Fig. 8(a), whose amplitude increases by 48.04% (5.14 A) compared with that in healthy conditions (3.47 A). The same situation repeats for $p = 3$ when the amplitude of i_1 rises from 6.72854 to 9.73 A, corresponding to an increase of 44.63%, as shown in Fig. 8(b). Finally, in controlled post-fault conditions, the developed controller achieves equal current amplitudes in the remaining healthy windings.

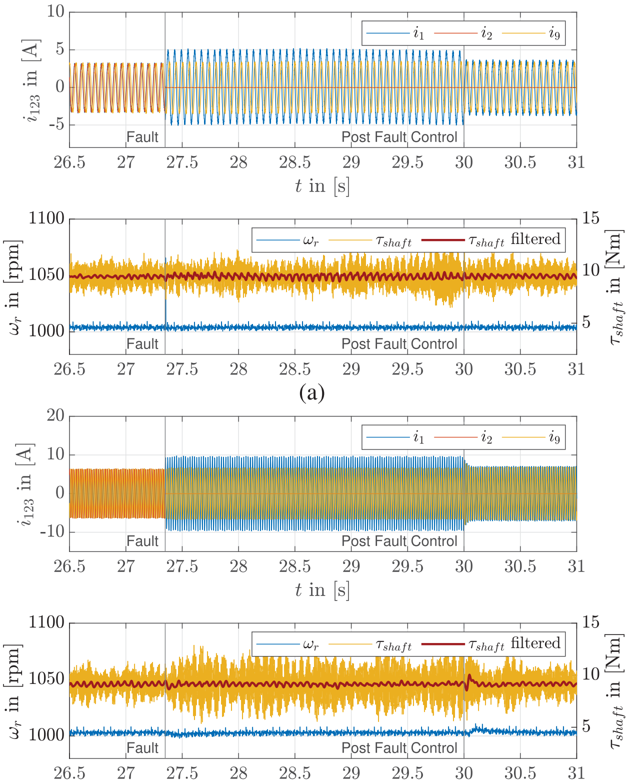

Fig. 8. Waveforms of the currents in windings 1, 2, and 9 of the VPM, τ_{shaft}, and ω_r before, during, and after an OPF in the second winding $(k_f = 2)$. Pole-phase configurations with (a) $[m = 18, p = 1]$ and (b) $[m = 6, p = 3]$.

Figs. 9 and 10 show the loci of the current space vector $\bar{i}_{\alpha\beta 0,h}$ in healthy, faulty, and post-fault controlled operating conditions when $p = 1$ and $p = 3$, respectively. In healthy operating conditions, shown in Figs. 9(a) and 10(a), the currents appear balanced in both PPCs in the torque-producing plane, while the currents $\bar{i}_{\alpha\beta 0,h}$ $(h \neq p)$ remain around zero in the non-excited planes. Figs. 9(b) and 10(b) show the imbalance in the $\alpha\beta 0$ harmonic planes caused by the fault. It can be noted that $\bar{i}_{\alpha\beta 0,h}$ has a non-negligible magnitude, which increases depending on the order of the harmonic plane. Moreover, the discrepancy between the blue and orange lines reveals that the direction of $\bar{i}_{\alpha\beta 0,h}$ may be far from the one preserving the motor torque. Even the locus of the current space vector $\bar{i}_{\alpha\beta 0,p}$ in the torque-producing harmonic plane deviates from its ideal circular trajectory. Then, Figs. 9(c) and 10(c) show that, when the fault-tolerant control strategy

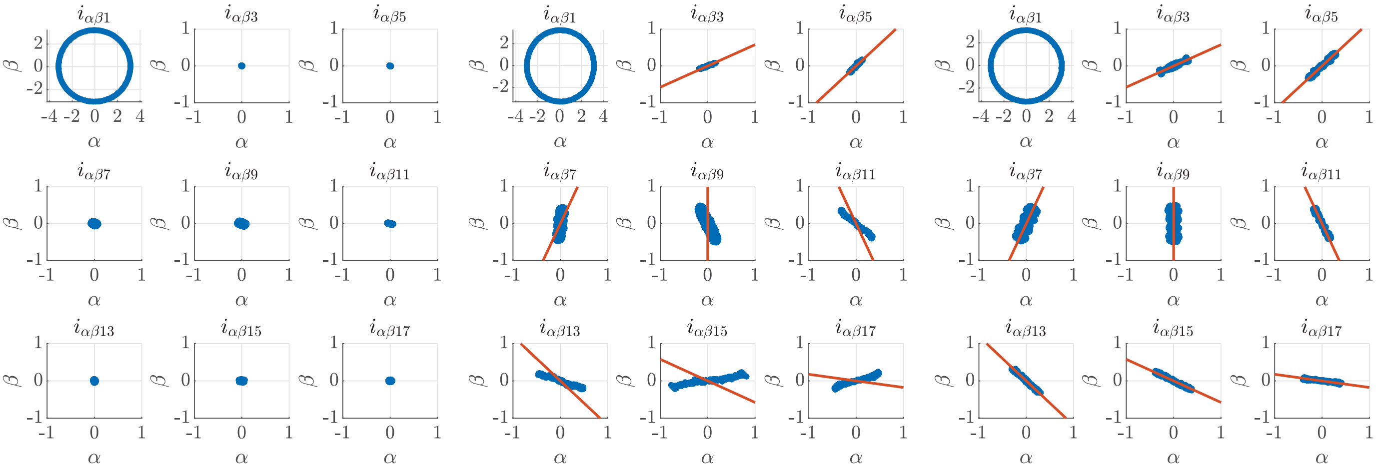

(a) (b) (c)

Fig. 9. Loci of the current space vector (blue) for a PPC with [$m = 18$, $p = 1$] in healthy, faulty, and post-fault controlled conditions in comparison with the expected direction of the loci (orange) in all harmonic planes for an OPF with $k_f = 2$. (a) Healthy [$m = 18$, $p = 1$]. (b) Faulty [$m = 18$, $p = 1$]. (c) Post-fault controlled [$m = 18$, $p = 1$].

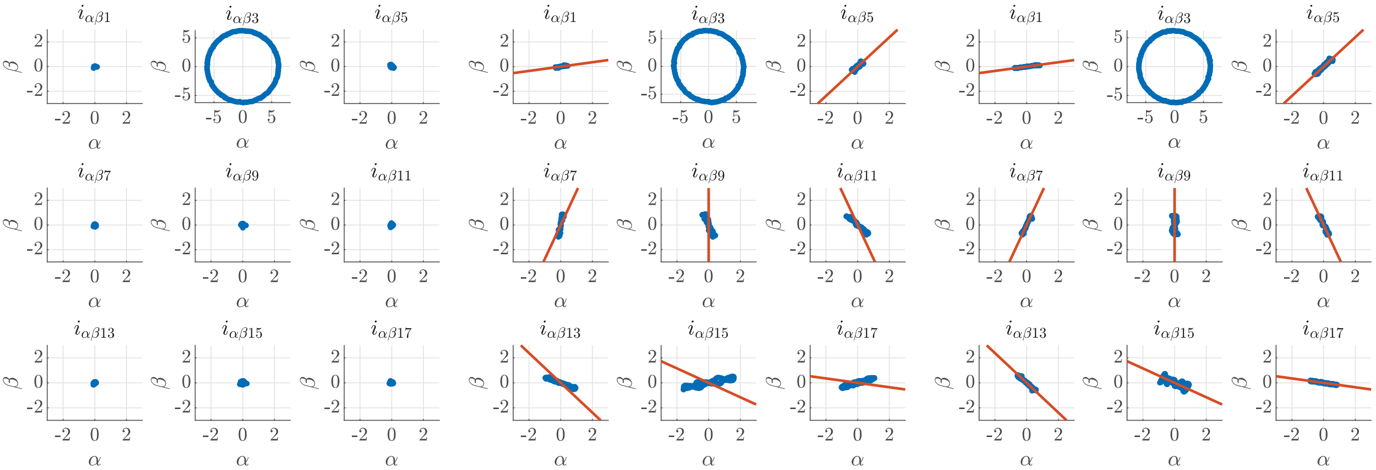

(a) (b) (c)

Fig. 10. Loci of the current space vector (blue) for the PPC with [$m = 6$, $p = 3$] in healthy, faulty, and post-fault controlled conditions, and expected directions of the loci (orange) for an OPF with $k_f = 2$. (a) Healthy [$m = 6$, $p = 3$]. (b) Faulty [$m = 6$, $p = 3$]. (c) Post-fault controlled [$m = 6$, $p = 3$].

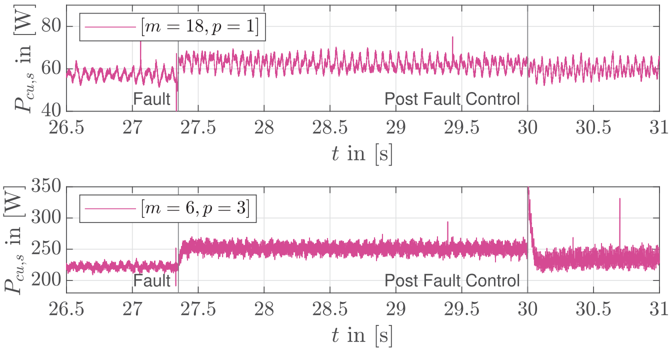

Fig. 11. Stator copper losses for both PPCs. A reduction while applying the PFC is observed.

is activated, the current space vectors $\bar{i}_{\alpha\beta 0,h}$ ($h \neq p$) follow the reference directions despite spurious high-order harmonics. It can also be seen that the magnitude of $\bar{i}_{\alpha\beta 0,h}$ is the same in all non-excited harmonic planes.

As explained in Section III, the proposed approach aims to reduce the stator copper losses $P_{\mathrm{cu},s}$ (7). Fig. 11 shows $P_{\mathrm{cu},s}$ calculated from the measured currents in both PPCs.

TABLE V

Average Stator Copper Losses for Both PPCs in Healthy, Faulty, and PFC Operation in Their Respective Steady States

[$m = 18, p = 1$]			[$m = 6, p = 3$]		
healthy	faulty	PFC	healthy	faulty	PFC
57.4 W	62.3 W	60.8 W	222 W	251 W	235 W

In addition, Table V juxtaposes the average $P_{\mathrm{cu},s}$ over 1 s for each operation condition. The PFC reduces the copper losses by 2.41% in the [$m = 18$, $p = 1$] case and 6.37% in the [$m = 6$, $p = 3$] case.

2) Pole Transition: Fig. 12 shows the $dq0$ currents under an OPF in the second phase ($k_f = 2$) during the transition from a PPC with [$m = 18$, $p = 1$] to a PPC with [$m = 6$, $p = 3$]. To simplify the visualization, the current vector $\bar{i}_{\alpha\beta 0,h\neq p}$ in the non-torque-producing planes is multiplied by $e^{-j\theta_{h,k_f}}$, and consequently, the resulting q component is zero. For the same reason, only the d component of $\bar{i}_{\alpha\beta 0,5}$ is shown. This figure stands exemplary for all unexcited harmonic planes.

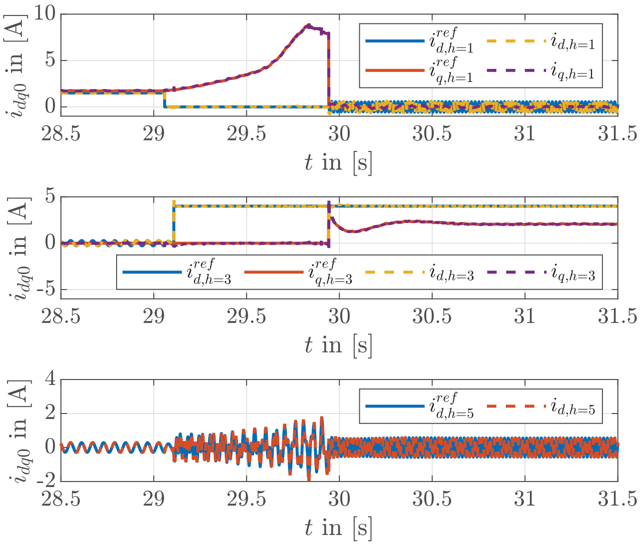

Fig. 12. Waveforms of $i_{d,1}$ and $i_{q,1}$ in plane $p_1 = 1$, $i_{d,3}$ and $i_{q,3}$ in plane $p_2 = 3$, and $i_{d,5}$ in the non-excited harmonic plane with $h = 5$ during a pole transition with an OPF ($k_f = 2$).

For $t < 29.1$ s, $i_{d,1}$ and $i_{q,1}$ appear undisturbed by the fault, while the d components of the currents in the other planes oscillate according to the developed post-fault strategy. For $29.1 \text{ s} < t < 29.9$ s, the pole change occurs. The magnetizing current $i_{d,1}$ drops, while $i_{d,3}$ increases up to its new reference value. Also, $\psi_{R,p_1=1}$ decreases with a first-order transient. As a result, $i_{q,1}$ increases to preserve the torque. Meanwhile, $\psi_{R,p_2=3}$ rises. At $t = 29.9$ s, $i_{q,1}$ is set to zero, and $i_{q,3}$ generates the torque.

Fig. 12 reveals that the currents in both harmonic planes ($p_1 = 1$ and $p_2 = 3$) follow their references adequately and do not contain significant harmonics even if simultaneously excited. In contrast, in steady state, the d-axis current in the non-excited harmonic plane (here, $h = 5$) shows a single-harmonic component at angular frequency ω_{s,p_1} before and ω_{s,p_2} after the pole changing. During the transition, a superposition of these two frequencies with varying amplitude is observed. Fig. 13 shows the time-domain currents of windings $[1, 2, 9]$ during the same pole transition. The top and bottom plots, corresponding to configurations with p_1 and p_3 pole pairs, respectively, show that the currents in the faulty winding are zero in steady-state conditions. Furthermore, the currents in healthy windings 1 and 9 are equal in amplitude and frequency. During the pole transition, a superposition of two harmonic frequencies is observable in the middle plot. Both the $dq0$ and the 123 reference frames confirm that the PIR controllers with two resonant frequencies achieve the fault tolerance for both PPCs simultaneously.

Finally, Fig. 14 shows the measured mechanical rotor speed ω_r and torque τ_{shaft} during the pole transition. In fault conditions, the speed error exceeds the 0.5 % band for $\tau_{s,0.5\ \%} \approx 0.75$ s. This transient is longer than the one reported in [15], but the tests cannot be directly compared because of the different machine configurations. Furthermore, a different pole transition was presented in [15], i.e., from one to four pole pairs. Nevertheless, this test demonstrates that pole changing is possible, even if the machine operates under an OPF.

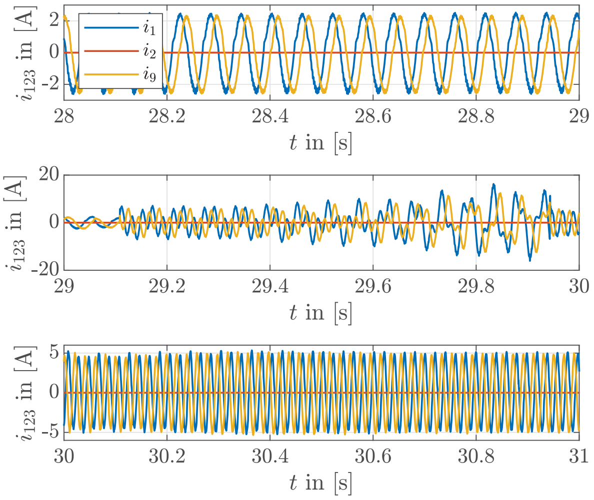

Fig. 13. Waveforms of the currents in windings $[1, 2, 9]$ during a pole transition with an OPF ($k_f = 2$). From top to bottom: initial steady state $[m = 18, p = 1]$, the pole transition, and final steady state $[m = 6, p = 3]$.

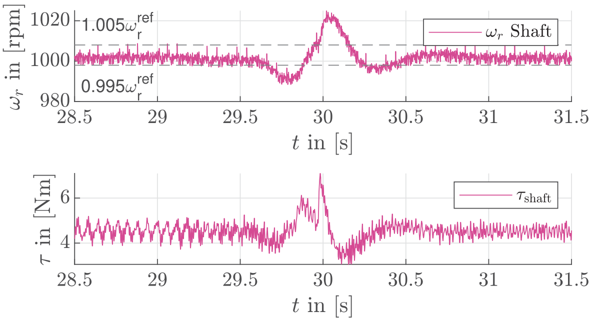

Fig. 14. Waveform of the measured rotor speed ω_r and shaft torque τ_{shaft} during the pole transition under an OPF ($k_f = 2$).

VI. CONCLUSION

This article proposes a PFC for an 18-phase VPM, which is capable of managing an OPF. The proposed solution can meet the high-reliability requirements of long-haul trucks and allows the vehicle to continue operating until maintenance is possible, substantially reducing the cost of the fault. The mathematical basis of the controller is the HPD theory, which provides a unified model for the control system. The PFC has been tested under steady-state and transient conditions. Its modular structure makes it easy to adapt to machines with a different number of phases. The experimental results demonstrate that the PFC can deliver constant torque operation with different pole pairs and perform pole transitions even under fault conditions, thereby achieving TFL.

ACKNOWLEDGMENT

The authors would like to pronounce their appreciation for the reviewers in contributing to improve this submission.

REFERENCES

[1] E. Levi, R. Bojoi, F. Profumo, H. A. Toliyat, and S. Williamson, "Multiphase induction motor drives—A technology status review," *IET Electr. Power Appl.*, vol. 1, no. 4, pp. 489–516, 2007. [Online]. Available: https://digital-library.theiet.org/content/journals/10.1049/iet-epa_20060342

[2] E. Levi, "Advances in converter control and innovative exploitation of additional degrees of freedom for multiphase machines," *IEEE Trans. Ind. Electron.*, vol. 63, no. 1, pp. 433–448, Jan. 2016. [Online]. Available: https://ieeexplore.ieee.org/document/7110356

[3] F. Barrero and M. J. Duran, “Recent advances in the design, modeling, and control of multiphase machines—Part I,” *IEEE Trans. Ind. Electron.*, vol. 63, no. 1, pp. 449–458, Jun. 2016. [Online]. Available: https://ieeexplore.ieee.org/document/7128683

[4] M. J. Duran and F. Barrero, “Recent advances in the design, modeling, and control of multiphase machines—Part II,” *IEEE Trans. Ind. Electron.*, vol. 63, no. 1, pp. 459–468, Jun. 2016. [Online]. Available: https://ieeexplore.ieee.org/document/7130602

[5] V. T. Buyukdegirmenci, A. M. Bazzi, and P. T. Krein, “Evaluation of induction and permanent-magnet synchronous machines using drive-cycle energy and loss minimization in traction applications,” *IEEE Trans. Ind. Appl.*, vol. 50, no. 1, pp. 395–403, Jan. 2014. [Online]. Available: https://ieeexplore.ieee.org/document/6524023

[6] V. Schwarzer and R. Ghorbani, “Drive cycle generation for design optimization of electric vehicles,” *IEEE Trans. Veh. Technol.*, vol. 62, no. 1, pp. 89–97, Jan. 2013.

[7] R. Raj, P. Subramaniyane, and L. Peretti, “Design of a variable phase-pole induction machine for electric vehicle applications,” in *Proc. Int. Conf. Electr. Mach. (ICEM)*, Sep. 2022, pp. 976–982.

[8] E. Libbos, B. Ku, S. Agrawal, S. Tungare, A. Banerjee, and P. T. Krein, “Loss minimization and maximum torque-per-ampere operation for variable-pole induction machines,” *IEEE Trans. Transport. Electrific.*, vol. 6, no. 3, pp. 1051–1064, Sep. 2020. [Online]. Available: https://ieeexplore.ieee.org/document/9099876

[9] E. Libbos, E. Krause, A. Banerjee, and P. T. Krein, “Inverter design considerations for variable-pole induction machines in electric vehicles,” *IEEE Trans. Power Electron.*, vol. 37, no. 11, pp. 13554–13565, Nov. 2022. [Online]. Available: https://ieeexplore.ieee.org/document/9779946

[10] S. Mallampalli, Z. Q. Zhu, J.-C. Mipo, and S. Personnaz, “48 V starter-generator induction machine with pole-changing windings,” *IEEE Trans. Ind. Appl.*, vol. 56, no. 6, pp. 6324–6337, Jul. 2020. [Online]. Available: https://ieeexplore.ieee.org/document/8912170

[11] S. Mallampalli, Z. Q. Zhu, J. C. Mipo, and S. Personnaz, “Six-phase pole-changing winding induction machines with improved performance,” *IEEE Trans. Energy Convers.*, vol. 36, no. 1, pp. 534–546, Mar. 2021. https://ieeexplore.ieee.org/document/9140298

[12] E. Libbos, E. Krause, A. Banerjee, and P. T. Krein, “Winding layout considerations for variable-pole induction motors in electric vehicles,” *IEEE Trans. Transport. Electrific.*, vol. 9, no. 4, pp. 5214–5225, Dec. 2023. [Online]. Available: https://ieeexplore.ieee.org/document/10050555

[13] E. Libbos, R. Hao, B. Ku, A. Banerjee, and P. T. Krein, “Modular multiphase drives for variable-pole induction machines in electric vehicles,” in *Proc. IEEE Appl. Power Electron. Conf. Expo. (APEC)*, Mar. 2020, pp. 696–703. [Online]. Available: https://ieeexplore.ieee.org/document/9124085/

[14] E. Libbos, B. Ku, S. Agrawal, S. Tungare, A. Banerjee, and P. T. Krein, “Variable-pole induction machine drive for electric vehicles,” in *Proc. IEEE Int. Electric Mach. Drives Conf. (IEMDC)*, May 2019, pp. 515–522. [Online]. Available: https://ieeexplore.ieee.org/document/8785212

[15] Y. Wu, G. F. Olson, and L. Peretti, “Pole-transition control of variable-pole machines using harmonic-plane decomposition,” *IEEE Trans. Ind. Electron.*, vol. 70, no. 8, pp. 7753–7760, Aug. 2023. [Online]. Available: https://ieeexplore.ieee.org/document/10002412

[16] G. F. Olson, Y. Wu, O. I. U. Haq, and L. Peretti, “Enabling variable phase-pole drives with the harmonic plane decomposition,” *IEEE Access*, vol. 12, pp. 40049–40063, 2024. [Online]. Available: https://ieeexplore.ieee.org/document/10464271

[17] S. Karugaba and O. Ojo, “A carrier-based PWM modulation technique for balanced and unbalanced reference voltages in multiphase voltage-source inverters,” *IEEE Trans. Ind. Appl.*, vol. 48, no. 6, pp. 2102–2109, Nov. 2012. [Online]. Available: https://ieeexplore.ieee.org/document/6339046

[18] L. Vancini, M. Mengoni, G. Rizzoli, G. Sala, L. Zarri, and A. Tani, “Carrier-based PWM overmodulation strategies for five-phase inverters,” *IEEE Trans. Power Electron.*, vol. 36, no. 6, pp. 6988–6999, Jun. 2021. [Online]. Available: https://ieeexplore.ieee.org/document/9241425

[19] W. Kong, R. Qu, M. Kang, J. Huang, and L. Jing, “Air-gap and yoke flux density optimization for multiphase induction motor based on novel harmonic current injection method,” *IEEE Trans. Ind. Appl.*, vol. 53, no. 3, pp. 2140–2148, May 2017. [Online]. Available: https://ieeexplore.ieee.org/document/7732512

[20] S. Yang, A. Bryant, P. Mawby, D. Xiang, L. Ran, and P. Tavner, “An industry-based survey of reliability in power electronic converters,” *IEEE Trans. Ind. Appl.*, vol. 47, no. 3, pp. 1441–1451, May 2011. [Online]. Available: https://ieeexplore.ieee.org/document/5316356

[21] G. Yang, S. Li, H. Hussain, J. Zhang, and J. Yang, “A novel SVPWM fault-tolerant strategy for torque ripple reduction of seven-phase induction machines under single-phase open-circuit fault,” *IEEE Trans. Power Electron.*, vol. 38, no. 4, pp. 5217–5229, Apr. 2023. [Online]. Available: https://ieeexplore.ieee.org/document/9999346

[22] A. Tani, M. Mengoni, L. Zarri, G. Serra, and D. Casadei, “Control of multiphase induction motors with an odd number of phases under open-circuit phase faults,” *IEEE Trans. Power Electron.*, vol. 27, no. 2, pp. 565–577, Feb. 2012. [Online]. Available: https://ieeexplore.ieee.org/document/5744128

[23] W. Kong, M. Kang, D. Li, R. Qu, D. Jiang, and C. Gan, “Investigation of spatial harmonic magnetic field coupling effect on torque ripple for multiphase induction motor under open fault condition,” *IEEE Trans. Power Electron.*, vol. 33, no. 7, pp. 6060–6071, Jul. 2018.

[24] B. Chikondra, U. R. Muduli, and R. K. Behera, “An improved open-phase fault-tolerant DTC technique for five-phase induction motor drive based on virtual vectors assessment,” *IEEE Trans. Ind. Electron.*, vol. 68, no. 6, pp. 4598–4609, Jun. 2021. [Online]. Available: https://ieeexplore.ieee.org/document/9089215

[25] A. A. Rockhill and T. A. Lipo, “A generalized transformation methodology for polyphase electric machines and networks,” in *Proc. IEEE Int. Electric Mach. Drives Conf. (IEMDC)*, May 2015, pp. 27–34. [Online]. Available: https://ieeexplore.ieee.org/document/7409032

[26] M. Jecmenica, B. Brkovic, E. Levi, and Z. Lazarevic, “Interplane cross-saturation in multiphase machines,” *IET Electric Power Appl.*, vol. 13, no. 11, pp. 1812–1822, Nov. 2019, doi: 10.1049/iet-epa.2018.5546.

[27] Y. Wu, G. F. Olson, C. Henriksson, and L. Peretti, “Open fault detection in variable phase-pole machines based on harmonic plane decomposition,” *IEEE Trans. Power Electron.*, vol. 39, no. 4, pp. 4557–4566, Apr. 2024. [Online]. Available: https://ieeexplore.ieee.org/document/10379138

[28] L. Harnefors, “Design and analysis of general rotor-flux-oriented vector control systems,” *IEEE Trans. Ind. Electron.*, vol. 48, no. 2, pp. 383–390, Apr. 2001. [Online]. Available: https://ieeexplore.ieee.org/document/915417

[29] D. G. Holmes, T. A. Lipo, B. P. McGrath, and W. Y. Kong, “Optimized design of stationary frame three phase AC current regulators,” *IEEE Trans. Power Electron.*, vol. 24, no. 11, pp. 2417–2426, Nov. 2009. [Online]. Available: https://ieeexplore.ieee.org/document/5338054

[30] G. F. Olson, Y. Wu, and L. Peretti, “Parameter estimation of multiphase machines applicable to variable phase-pole machines,” *IEEE Trans. Energy Convers.*, vol. 38, no. 4, pp. 2822–2831, Dec. 2023. [Online]. Available: https://ieeexplore.ieee.org/document/9910883

[31] ABB. *3GAA161420-BDG*. Accessed: Oct. 31, 2022. [Online]. Available: https://new.abb.com/products/sv/3GAA161420-BDG/3gaa161420-bdg

[32] Analog Devices. *AD9249*. Accessed: Mar. 20, 2024. [Online]. Available: https://www.analog.com/en/products/ad9249.html?doc=AD9249.pdf

[33] Advanced Micro Devices. (2022). *Xilinx Zynq-7000 SoC ZC706 Evaluation Kit*. [Online]. Available: https://www.xilinx.com/products/boards-and-kits/ek-z7-zc706-g.html

[34] Magtrol. *TM Series—Torque Sensors*. Accessed: May 25, 2023. [Online]. Available: https://www.magtrol.com/product/torque-transducers/

[35] Magtrol. *3411—Torque Display*. Accessed: May 25, 2023. [Online]. Available: https://www.magtrol.com/product/model-3411-torque-display/

[36] Tektronix. *3 Series MDO Mixed Domain Oscilloscope*. Accessed: May 25, 2023. [Online]. Available: https://www.tek.com/en/products/oscilloscopes/3-series-mdo

Yixuan Wu (Graduate Student Member, IEEE) received the M.Sc. degree in electrical engineering from RWTH Aachen University, Aachen, Germany, and the KTH Royal Institute of Technology, Stockholm, Sweden, in 2019, where he is currently pursuing the Ph.D. degree in fault tolerance in multiphase electrical machines with the Division of Electrical Power and Energy Systems (EPE).

His research interests include modeling and control of variable phase-pole drives, power electronics, fault tolerance, and electromobility.

Luca Vancini (Member, IEEE) received the M.Sc. and Ph.D. degrees in electrical engineering from the University of Bologna, Bologna, Italy, in 2018 and 2022, respectively.

He is currently a Research Fellow with the Department of Electric, Electronic and Information Engineering "Guglielmo Marconi," University of Bologna. His research interests include power electronics, control of multiphase converters, and diagnostic techniques for multiphase machines.

Luca Zarri (Senior Member, IEEE) received the M.Sc. and Ph.D. degrees in electrical engineering from the University of Bologna, Bologna, Italy, in 1998 and 2007, respectively.

He is currently a Full Professor of power electronics, and electrical machines and drives with the Department of Electrical, Electronic and Information Engineering "Guglielmo Marconi," University of Bologna. He has authored or coauthored more than 170 scientific articles. His research activity concerns the control of power converters and electric drives.

Dr. Zarri is a Senior Member of the IEEE Industry Applications, IEEE Power Electronics, and IEEE Industrial Electronics Societies. He serves as the Vice Chair for the IAS Industrial Power Systems Conversion Department.

Angelo Tani received the M.Sc. degree (Hons.) in electrical engineering from the University of Bologna, Bologna, Italy, in 1988.

He is currently a Full Professor of power electronics, and electrical machines and drives with the Department of Electrical, Electronic and Information Engineering "Guglielmo Marconi," University of Bologna. He has authored more than 200 articles published in technical journals and conference proceedings. His current activities include modeling, control, and fault diagnosis of multiphase electric machines.

Luca Peretti (Senior Member, IEEE) received the M.Sc. degree in electronic engineering from the University of Udine, Udine, Italy, in 2005, and the Ph.D. degree in electrical drives for application in mechatronics from the University of Padova, Padua, Italy, in 2009.

From November 2007 to March 2008, he was a Visiting Ph.D. Student with ABB Corporate Research, Västerås, Sweden. From August 2010 to August 2018, he was with ABB Corporate Research, in different roles as a Principal Scientist, the Project Leader, and a Strategy Coordinator. He has been an affiliated Faculty Member with KTH, Stockholm, Sweden, Division of Electric Power and Energy Systems, since July 1, 2016. Since September 2018, he has been an Associate Professor with KTH, Division of Electric Power and Energy Systems, in the field of electric machines and drives. His main scientific research interests include the automatic parameter estimation in electric machines, sensorless control, loss segregation in drive systems, multiphase drives, and condition monitoring of machines and drives, in the context of industrial, wind energy, and traction applications.

Open Access funding provided by 'Alma Mater Studiorum - Università di Bologna' within the CRUI CARE Agreement